Journal of Materials Chemistry C

ROYAL SOCIETY OF CHEMISTRY

PAPER

View Article Online
View Journal | View Issue

Cite this: J. Mater. Chem. C, 2021, 9, 15608

Luminescent solar concentrators with outstanding optical properties by employment of D–A–D quinoxaline fluorophores†

Costanza Papucci,[abc] Rima Charaf,[d] Carmen Coppola,[ce] Adalgisa Sinicropi,[ace] Mariangela di Donato,[af] Maria Taddei,[af] Paolo Foggi,[fgh] Antonella Battisti,[i] Bastiaan de Jong,[cj] Lorenzo Zani,[a] Alessandro Mordini,[ab] Andrea Pucci,[*ad] Massimo Calamante[*ab] and Gianna Reginato[*a]

Luminescent solar concentrators (LSCs) are devices designed to efficiently collect both direct and diffuse solar radiation and concentrate it on photovoltaic cells to foster their use in building-integrated photovoltaics (BIPV). The optimization of LSC performances involves the adjustment of both the fluorophore and the guest polymer matrix. On this account, we investigated a series of high quantum yield, donor–acceptor–donor (D–A–D) photostable fluorophores (**DQ1–5**), presenting a central quinoxalinic acceptor core, not previously employed in LSCs, and triarylamines or phenothiazine as donor groups. The molecules were also decorated with alkyl chains on the central core and/or the donor groups, to explore their compatibility with the poly(methyl methacrylate) (PMMA) and poly(cyclohexyl methacrylate) (PCMA) matrices utilized in this study. The PMMA and PCMA films (25 μm thick), containing 0.2–2.2 wt% of **DQ1–5,** absorbed in the 370–550 nm range and presented emission maxima at 550–600 nm, with fluorescence quantum yields higher than 40% even at the highest doping contents. Notably, the **DQ1**/PMMA thin-films showed enhanced phase compatibility and excellent quantum yields, *i.e.*, >95%. Accordingly, they were designed to obtain 25 cm^2 area LSCs with remarkable internal (η_{int}) and external (η_{ext}) photon efficiencies of 42.9% and 6.2%, respectively, higher than those observed from state-of-the-art devices based on the Lumogen Red 305 (**LR305**) as the reference fluorophore. Overall, these were the best results ever achieved in our laboratory for thin-film LSCs built with organic fluorescent emitters.

Received 23rd June 2021,
Accepted 10th October 2021

DOI: 10.1039/d1tc02923a

rsc.li/materials-c

1. Introduction

In the past few decades, the need to reduce CO_2 emissions generated by human activities has prompted the scientific community to study new and efficient methods to utilize renewable energy sources, such as sunlight, for power generation, aiming to progressively replace the use of fossil fuels.[1] Among the currently available technologies, silicon photovoltaics (Si-PVs) have been the subject of continuous development efforts, which ultimately led to the reduction in the production prices of the modules at an actual electricity cost of about 0.2 $ per Watt peak (Wp)[2] without detrimenting performances.

Nevertheless, Si-PV panels provide the maximum efficiency only under direct light irradiation and require an efficient dissipation of the excess heat due to the unconverted energy. Luminescent solar concentrators (LSCs) rely on a technology studied since the 1970s[3,4] and were developed with the aim of obtaining large-area, semi-transparent and cheap photovoltaic devices capable of concentrating both direct and diffuse solar

[a] Institute of Chemistry of Organometallic Compounds (CNR-ICCOM), Via Madonna del Piano 10, 50019 Sesto Fiorentino, Italy
[b] Department of Chemistry "U. Schiff", University of Florence, Via della Lastruccia 13, 50019 Sesto Fiorentino, Italy
[c] Department of Biotechnology, Chemistry and Pharmacy, University of Siena, Via A. Moro 2, 53100 Siena, Italy
[d] Department of Chemistry and Industrial Chemistry, University of Pisa, Via G. Moruzzi 13, 56124 Pisa, Italy
[e] CSGI, Consorzio per lo Sviluppo dei Sistemi a Grande Interfase, 50019 Sesto Fiorentino, Italy
[f] LENS, European Laboratory for Non-Linear Spectroscopy, via N. Carrara 1, 50019 Sesto Fiorentino, Italy
[g] Department of Chemistry, Biology and Biotechnology, University of Perugia, via Elce di Sotto 8, 06123 Perugia, Italy
[h] INRIM (Istituto Nazionale di Scienza Metrologica), Strada delle Cacce 91, 10135 Torino, Italy
[i] Nanoscience Institute, CNR and NEST, Scuola Normale Superiore, P.zza S. Silvestro 12, 56127 Pisa, Italy
[j] Cicci Research s.r.l., Via Giordania 227, 58100 Grosseto, Italy

† Electronic supplementary information (ESI) available. See DOI: 10.1039/d1tc02923a

radiation on small solar cells at their edges. Specifically, they consist of a panel of a common plastic material (*e.g.*, poly(methyl methacrylate), PMMA) containing a fluorescent dopant capable of absorbing direct and indirect sunlight and emitting it at longer wavelengths. Commonly used fluorescent compounds can be quantum dots, perovskites, rare-earth complexes and organic molecules.[5] The emitted radiation is mainly concentrated, *via* total internal reflection, at the edge of the panel (where the solar cells are placed) thanks to the different refractive indexes of air and the plastic material. This, together with the aesthetic characteristics of LSCs (color and shape tunability), supports their use in building-integrated photovoltaics (BIPVs).[6]

In order to obtain high-performance LSC devices, a careful study of the materials used for their assembly must be performed, concerning both the selection of the fluorophore and the plastic material in which it is dispersed.[5] Regarding the fluorophore, the most critical parameters influencing the final properties of the device are its fluorescence quantum yield (Φ_f) and Stokes shift (SS) which, together with the match between its emission spectrum and the electronic band-gap of the PV cell, govern the efficiency of the solar collector.

These properties, particularly Φ_f, can depend on the polarity of the medium (solution or polymer) in which the fluorophore is dispersed. For the polymer matrix, the main factor to be considered is its ability to disperse large amounts of fluorophores to promote solar harvesting, without activating fluorescence quenching phenomena due to aggregation[7,8] (aggregation caused quenching – ACQ). Furthermore, a good matrix might be able to affect the stability of the fluorophore excited state and thus enhance its fluorescence quantum yield. Clearly, a smart selection of the polymer, specifically tailored to fit the fluorophore properties, is an important factor for improving the device performance.

Among the different kinds of fluorophores applicable in LSCs, small organic molecules with a donor–acceptor type (D–A) structure, whose excitation determines the formation of a charge-transfer state with a significant dipole moment,[9] appear particularly interesting. We recently investigated the properties of a series of organic fluorophores with donor–acceptor–donor (D–A–D) structures, presenting a benzo[1,2-*d*:4,5-*d*′]bisthiazole acceptor core, dispersed in three methacrylic polymer matrices of different polarity.[10] Notably, we found that by decreasing the polarity of the matrix by passing from PMMA to poly(cyclohexyl methacrylate) (PCMA, Fig. 1), the Φ_f of the molecules increased due to the decreased stabilization of the charge-transfer excited state, resulting in a superior optical efficiency of the corresponding LSCs.

To further explore the interactions between organic emitters and polymer matrices of varying polarity and assess their effects on the performances of the corresponding LSCs, we decided to investigate a different series of luminophores, still presenting the same D–A–D architecture. We focused on quinoxaline, a molecular scaffold which is quite easy to functionalize and is characterized by good light harvesting ability, high Φ_f and large SS.[11–18]

Owing to their photophysical properties, quinoxalines are good candidates for application in LSCs but, although they have been extensively applied in organic optoelectronics,[19] their use in such devices has not yet been reported. Therefore, starting from a previously reported compound, **DQ1**,[20,21] a series of symmetrical derivatives were designed and synthesized by modifying both the donor groups at the 5,8 positions and the substituents at the 2,3 positions (Fig. 1).

The optical properties of the new molecules were investigated in solution and after dispersion in the PMMA and PCMA matrices to determine their absorption and emission features as well as their Φ_f. Furthermore, transient absorption spectroscopy (TAS) and fluorescence lifetime studies were also carried out to monitor the excited state evolution and correlate the device characteristics with the dynamic optical properties of the fluorophores. Due to the outstanding performances of these emitters also when dispersed into polymers, LSCs presented excellent optical properties, even superior to those found using the commercial reference fluorophore Lumogen Red 305 (**LR305**).[5,8,10]

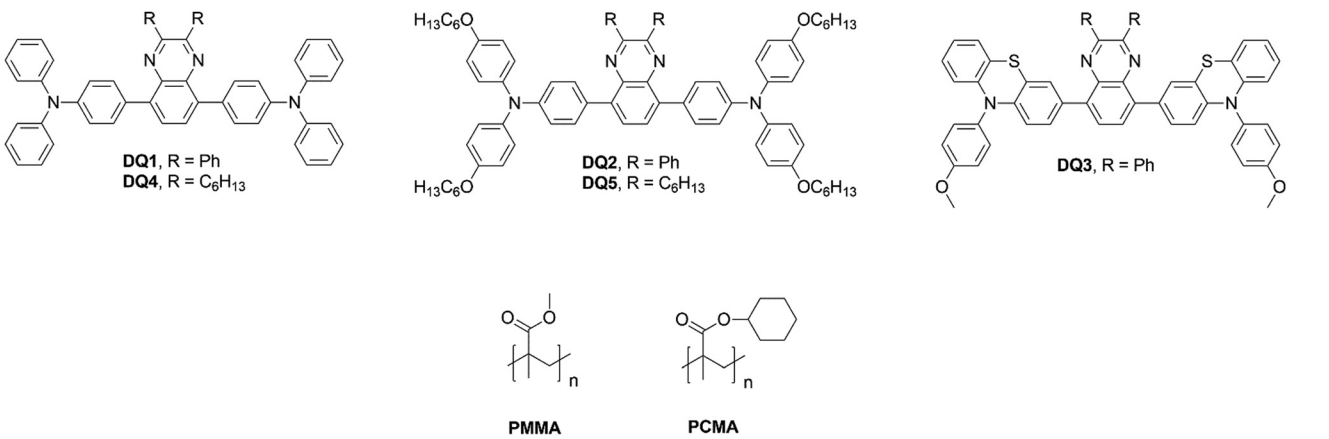

Fig. 1 Chemical structure of fluorophores based on 2,3-diphenyl-quinoxaline (**DQ1-3**) or 2,3-dihexyl-quinoxaline (**DQ4-5**) acceptor cores and of the used polymer matrices.

2. Experimental

2.1 General remarks

All commercially available compounds were purchased from Merck KgaA, Fluorochem Ltd and T.C.I. Co. Ltd, and were used without further purification unless stated otherwise. Anhydrous toluene was obtained after drying with a PureSolv Micro apparatus (Inert). Organometallic reactions were carried out under dry nitrogen using Schlenk techniques. Solvent degassing was carried out according to the ''freeze–pump–thaw'' method. Reactions were monitored by TLC on Kieselgel 60 F254 (Merck) aluminium sheets and the products were visualized by exposing the plate to UV light or by staining it with $KMnO_4$ solution. Flash column chromatography was performed using a Merck Kieselgel 60 (300–400 mesh) as the stationary phase. ^{1}H-NMR spectra were recorded at 200–400 MHz, and ^{13}C-NMR spectra were recorded at 50.3–100.6 MHz, using Varian Gemini/Mercury/INOVA series instruments. Chemical shifts (δ) are reported in parts per million (ppm) and are referenced to the residual solvent peak ($CDCl_3$, δ = 7.26 ppm for ^{1}H-NMR and δ = 77.0 ppm for ^{13}C-NMR; CD_2Cl_2, δ = 5.32 ppm for ^{1}H-NMR and δ = 53.84 ppm for ^{13}C-NMR), while coupling constants (J) are reported in Hz. ESI-MS spectra were obtained by direct injection of the sample solution using a Thermo Scientific LCQ-FLEET instrument, while HRMS spectra were measured using a Thermo Scientific LTQ Orbitrap (FT-MS) instrument (carried out at the Interdepartmental Centre for Mass Spectrometry of the University of Florence, CISM); main peaks for both are reported in the form m/z.

2.2 Spectroscopic analysis in solution

UV-vis absorption spectra were recorded with a Shimadzu 2600 series spectrometer, and fluorescence spectra were recorded with a JASCO FP-8300 spectrofluorometer, irradiating the sample at the wavelength corresponding to maximum absorption in the UV-vis spectrum. Absolute fluorescence quantum yields (Φ_f) in toluene solution were determined at room temperature using an integration sphere.

2.3 LSC film preparation

Polymer thin films containing the selected fluorophore were prepared by pouring 1.5 mL of toluene (Sigma-Aldrich, HPLC Plus, $\geq$99.9%) solution containing about 60 mg of the polymer and different concentrations (0.2–2.2 wt%) of the fluorophore on a 50 × 50 × 3 mm optically pure glass substrate (Edmund Optics Ltd BOROFLOAT window 50 × 50 TS). The amount of fluorophore was taken from a mother solution at a concentration of 1.5 mg mL^{-1}. The glass slides were cleaned with chloroform and immersed in 6M HCl for at least 12 h and then dried according to previously reported procedures.[22–27] Fluorophore-doped polymer thin films with a thickness of 25 ± 5 μm (Starrett micrometer) were obtained after complete evaporation of toluene at room temperature under a saturated atmosphere of chloroform (Merck, ACS reagent, $\geq$99.8%). After LSC characterization, the polymer films were carefully detached from the glass surface by immersing the LSC in water, stored in a desiccator and then analysed by means of absorption and emission spectroscopies.

2.4 Spectroscopic analysis of polymer films

UV-vis absorption spectroscopy on polymer films was performed at room temperature by using an Agilent Cary 5000 spectrophotometer. Fluorescence spectra on polymer films were recorded at room temperature with a Horiba Jobin-Yvon Fluorolog®-3 spectrofluorometer equipped with a 450 W xenon arc lamp and double-grating excitation and single-grating emission monochromators. Fluorescence quantum yields (Φ_f) in the solid state were determined using a 152-mm-diameter ''Quanta-φ'' integrating sphere, coated with Spectralon® and following the procedures reported earlier.[22,28,29] Epifluorescence microscopy was accomplished using a LED epifluorescence microscope (Schaefer South-East Europe S.r.l., Rovigo, Italy) equipped with a LED blue and green 5W light source and a DeltaPix Invenio 2EIII microscope camera (DeltaPix, Smorum, Denmark).

2.5 Transient absorption spectroscopy and fluorescence lifetime imaging (FLIM)

Ultrafast transient absorption spectra of all samples have been recorded on a system consisting of a home-built Ti:sapphire laser oscillator and regenerative amplifier system (Amplitude Pulsar) which produced 80 femtoseconds pulses at 810 nm with an average output power of 450–500 mW. Excitation pulses at 400 nm were obtained by the second harmonic generation of the fundamental laser output in a *2 mm-thick β-barium borate (BBO)* crystal. For all measurements, the pump beam polarization was set at the magic angle with respect to the probe beam by rotating a $\lambda/2$ plate to exclude rotational contributions to the transient signal.[30,31] The excitation powers were on the order of 50–100 nJ. The probe pulses were generated by focusing a portion of the 800 nm radiation beam on a *3 mm-thick CaF_2* window. The time delay between the pump and probe pulses was introduced by sending the portion of 800 nm light used for probe generation through a motorised stage. After passing through the sample, the white light probe was sent to a flat field monochromator coupled to a home-made CCD detector. For samples in solution, measurements were performed in a quartz cell (2 mm thick) mounted on a movable stage in order to refresh the solution and avoid undesired photochemical degradation of the sample. In the case of samples dispersed in PMMA, the polymeric films were directly mounted on the same motorised stage used for liquid samples. Analysis of the transient data was performed applying singular value decomposition (SVD)[32] and global analysis,[33] using GLOTARAN software.[34] Global analysis allows the simultaneous fit of all the measured wavelengths with a combination of exponential decay functions and retrieves the kinetic constants describing the dynamic evolution of the system and the corresponding spectral component, called evolution associated difference spectra (EADS). A linear decay kinetic scheme was employed for data analysis.

Fluorescence lifetime imaging (FLIM) was carried out on PMMA films doped with fluorophores **DQ1–5** (1.0 wt%) using a inverted confocal microscope Leica TCS SP5 (Leica Microsystems, Wetzlar, GE) coupled with an external pulsed diode laser (λ_{ex} = 405 nm) and a TCSPC acquisition card (PicoHarp 300, PicoQuant,

Berlin, GE) connected to internal spectral detectors. The laser repetition rate was set to 20 or 40 Hz. The images (256 × 256 pixels) were usually acquired with a scan speed of 400 Hz (lines per second). The pinhole aperture was adjusted depending on the fluorescence intensity and films were imaged under a 40×/NA 0.60 dry objective (Leica Microsystems). Fluorescence emission was monitored in the 480 and 620 nm range using the built-in acousto-optical beam splitter detection system of the microscope. Acquisitions were stopped after the collection of about 100–200 photons per pixel, at a photon counting rate of about 200–300 kHz. The decay curves were obtained from the binned lifetime images and fitted using PicoQuant SymPhoTime software.

2.6 Determination of LSC optical properties

Internal (η_{int}) and external (η_{ext}) photon efficiencies were evaluated in agreement with recent protocols[35] (see the ESI† for additional discussion and pictures). All the measurements were performed using a commercially available system (Arkeo – Cicci research s.r.l.) containing a CMOS-based spectrometer with a symmetrical Czerny–Turner optical bench connected to an integrating sphere. A fiber-based tunable LED source was used to excite the center of the LSC device with a circular spot of 2 mm in diameter and at a distance of 0.5 mm. The platform includes a tunable LED source composed of 10 monochromatic diodes (from 360 to 960 nm) and 2 white diodes (warm and cold) used to match AM 1.5G (Fig. S22 and S23, ESI†). The use of LED source allowed the irradiation stability with time. An integrating sphere of 5 cm of diameter and 1 cm of aperture is placed along the edge of the glass plate, such that the aperture of the sphere is fully covered by the glass and one corner coincides with the edge of the aperture hole. The integrating sphere was moved along the side of the LSC until all the slab edges had been scanned. The spectrally resolved edge output photon count was collected from the CMOS-based spectrometer and calibrated into optical power (W) and then in irradiance. Aimed at limiting reflections of unabsorbed light, an absorbing matte black background was placed in contact with the LSC rear side. The fiber was kept close and perpendicular to the centre of the LSC front surface to minimize the diverge of the excitation beam and to avoid the direct illumination of the integrating sphere.[36] A series of 3–5 measurements were repeated in order to align the integration sphere to collect the maximum single-edge output power. For the auto-absorption experiments, the Arkeo platform included a motorised translation stage and was equipped with a 405 nm, 1 mW laser.

2.7 Synthesis of DQs

4,4′-(2,3-Diphenylquinoxaline-5,8-diyl)bis(*N*,*N*-diphenyl) aniline, DQ1. In a Schlenk tube, under an inert atmosphere of nitrogen, Pd(dppf)Cl_2 (18 mg, 0.023 mmol, 10 mol%) was added to a solution of 5,8-dibromo-2,3-diphenylquinoxaline **5** (100 mg, 0.23 mmol, 1.0 eq.) in toluene/MeOH 6 : 1 (4 mL). KF (39 mg, 0.68 mmol, 3.0 eq.) and boronic acid **7** (164 mg, 0.57 mmol, 2.5 eq.) were added to the mixture. The solution was heated at 80 °C for 18 h. The mixture was then cooled at room temperature and water (5 mL) was added. The mixture was extracted with EtOAc (3 × 4 mL). The organic phase was washed with water and brine and then dried on anhydrous Na_2SO_4. Purification by flash column chromatography (SiO_2, petroleum ether/DCM 3 : 1) gave product **DQ1** as an orange solid (37 mg, 0.048 mmol, 21%). ^{1}H-NMR (400 MHz, $CDCl_3$): δ = 7.89 (s, 2H), 7.80 (d, J = 8.4 Hz, 4H), 7.63 (d, J = 7.6 Hz, 4H), 7.27–7.38 (m, 14H), 7.20–7.27 (m, 12H), 7.07 (dd, J = 7.6, 6.4 Hz, 4H) ppm. ^{13}C-NMR (100 MHz, $CDCl_3$): δ = 151.0, 147.7, 147.3, 139.1, 138.6, 138.4, 132.1, 131.7, 130.1, 129.4, 129.3, 128.8, 128.2, 124.7, 123.0, 122.7 ppm. HRMS: m/z calculated for $C_{56}H_{41}N_4$: 769.3326. Found: 769.3315 $[M + H]^+$.

General procedure for microwave-activated Suzuki–Miyaura cross coupling

In a microwave tube, Pd(dppf)Cl_2 (10 mol%) was added to a solution of appropriate dibromoquinoxaline (1.0 eq.) in toluene. Meanwhile, in a Schlenk tube, under a nitrogen atmosphere, boronic ester/acid (2.5 eq.) and KF (3.0 eq.) were dissolved in MeOH. After complete dissolution, the latter solution was added into the MW tube. The mixture was stirred for 30′ at room temperature and then heated under MW irradiation at 70 °C for 35′. The mixture was cooled at room temperature and the solvent was removed under a vacuum.

4,4′-(2,3-Diphenylquinoxaline-5,8-diyl)bis(*N*,*N*-bis(4-(hexyloxy)) phenyl)aniline, DQ2. 5,8-Dibromo-2,3-diphenylquinoxaline **5** (86 mg, 0.11 mmol, 1.0 eq.), Pd(dppf)Cl_2 (8.0 mg, 0.011 mmol, 10 mol%) in toluene (3 mL), boronic ester **8**[37] (157 mg, 0.27 mmol, 2.5 eq.) and KF (19 mg, 0.33 mmol, 3.0 eq.) in MeOH (0.5 mL) were reacted following the above general procedure. The crude product was purified by flash column chromatography (SiO_2, petroleum ether/DCM 5 : 1 → 3 : 1) obtaining **DQ2** as an orange solid (28 mg, 0.024 mmol, 21%). ^{1}H-NMR (400 MHz, $CDCl_3$): δ = 7.86 (s, 2H), 7.69 (d, J = 9.0 Hz, 4H), 7.58 (d, J = 7.4 Hz, 4H), 7.37–7.29 (m, 6H), 7.15 (d, J = 9.0 Hz, 8H), 7.04 (d, J = 11.9 Hz, 4H), 6.88 (d, J = 9.1 Hz, 8H), 3.96 (t, J = 6.4 Hz, 8H), 1.83–1.74 (m, 8H), 1.52–1.44 (m, 8H), 1.40–1.33 (m, 16H), 0.93 (t, J = 6.6 Hz, 12H) ppm. ^{13}C-NMR (100 MHz, $CDCl_3$): δ = 155.8, 151.1, 148.4, 140.4, 139.2, 138.3, 131.3, 129.9, 129.8, 129.15, 128.6, 128.1, 127.0, 118.9, 115.2, 68.3, 31.6, 29.3, 25.7, 22.6, 13.8 ppm. HRMS: m/z calculated for $C_{80}H_{89}O_4N_4$: 1169.6878. Found: 1169.6864 $[M + H]^+$.

3,3′-(2,3-Diphenylquinoxaline-5,8-diyl)bis(10-(4-methoxyphenyl))-10*H*-phenothiazine, DQ3. 5,8-Dibromo-2,3-diphenylquinoxaline **5** (174 mg, 0.23 mmol, 1.0 eq.), Pd(dppf)Cl_2 (16.8 mg, 0.023 mmol, 10 mol) in toluene (3 mL), boronic ester **9**[10] (248 mg, 0.57 mmol, 2.5 eq.) and KF (40 mg, 0.69 mmol, 3.0 eq.) in MeOH (0.5 mL) were reacted following the above general procedure. The crude product was purified by flash column chromatography (SiO_2, petroleum ether/DCM 4 : 1 → 2 : 1) obtaining **DQ3** as a yellow solid (93 mg, 0.10 mmol, 46%). ^{1}H-NMR (400 MHz, $CDCl_3$): δ = 7.74 (s, 2H), 7.59 (dd, J = 6.0, 3.6 Hz, 6H), 7.36 (d, J = 6.0 Hz, 4H), 7.33–7.29 (m, 8H), 7.15 (dd, J = 7.6, 3.2 Hz, 4H), 7.03 (dd, J = 5.6, 1.6 Hz, 2H), 6.82 (ddd, J = 9.2, 4.0, 1.2 Hz, 4H), 6.30 (d, J = 8.8 Hz, 2H), 6.19 (dd, J = 4.0, 2.0 Hz, 2H), 3.92 (s, 6H) ppm. ^{13}C-NMR (100 MHz, $CDCl_3$): δ = 159.2, 151.1, 144.4, 144.0, 138.3, 137.5, 133.2, 132.3, 132.2, 130.1, 129.1, 128.8, 128.7, 128.2, 126.8, 126.6, 122.3, 119.5, 118.9, 115.9,

115.6, 115.2, 55.5 ppm. HRMS: *m*/*z* calculated for $C_{58}H_{57}N_4$: 889.2665. Found: 889.2652 $[M + H]^+$.

4,4′-(2,3-Dihexylquinoxaline-5,8-diyl)bis(*N*,*N*-diphenyl)aniline, DQ4. 5,8-Dibromo-2,3-dihexylquinoxaline **6** (66 mg, 0.14 mmol, 1.0 eq.), $Pd(dppf)Cl_2$ (10.2 mg, 0.014 mmol, 10 mol%) in toluene (3 mL), boronic acid **7** (101 mg, 0.35 mmol, 2.5 eq.) and KF (24.4 mg, 0.42 mmol, 3.0 eq.) in MeOH (0.5 mL) were reacted following the above general procedure. The crude product was purified by flash column chromatography (SiO_2, petroleum ether/DCM 4 : 1 → 2 : 1 → EtOAc) obtaining **DQ4** as a yellow solid (67 mg, 0.08 mmol, 55%). ^{1}H-NMR (400 MHz, $CDCl_3$): δ = 7.77 (s, 2H), 7.72 (d, J = 8.4 Hz, 4H), 7.29 (dd, J = 15.9, 8.0 Hz, 8H), 7.24–7.15 (m, 12H), 7.04 (m, 4H), 2.97 (t, J = 7.6 Hz, 4H), 1.91–1.81 (m, 4H), 1.46–1.37 (m, 4H), 1.36–1.21 (m, 6H), 0.86 (t, J = 6.0 Hz, 6H) ppm. ^{13}C-NMR (100 MHz, $CDCl_3$): δ = 155.1, 148.0, 147.1, 138.8, 138.3, 132.9, 131.8, 129.4, 128.5, 124.7, 123.0, 34.9, 32.0, 29.3, 27.3, 22.8, 14.2 ppm. HRMS: *m*/*z* calculated for $C_{56}H_{57}N_4$: 785.4577. Found: 785.4564 $[M + H]^+$.

4,4′-(2,3-Dihexylquinoxaline-5,8-diyl)bis(*N*,*N*-bis(4-(hexyloxy) phenyl)aniline), DQ5. In a Schlenk tube, under an inert atmosphere of nitrogen, $Pd(PPh_3)_4$ (13 mg, 0.011 mmol, 10 mol%) was added to a solution of 5,8-dibromo-2,3-dihexylquinoxaline **6** (50 mg, 0.11 mmol, 1.0 eq.) in toluene (4 mL). Cs_2CO_3 (116 mg, 0.33 mmol, 3.0 eq.) and appropriate boronic ester **8**[37] (132 mg, 0.23 mmol, 2.1 eq.) were added to the mixture. The solution was heated at 110 °C for 4 h. The mixture was cooled at room temperature, water (5 mL) was added and the resulting solution was extracted with EtOAc (3 × 4 mL). The organic phase was washed with water and brine and then dried on anhydrous Na_2SO_4. The crude product was purified by flash column chromatography (SiO_2, petroleum ether/DCM 3 : 1 → 1 : 1) obtaining **DQ5** as an orange solid (108 mg, 0.091 mmol, 83%). ^{1}H-NMR (400 MHz, $CDCl_3$): δ = 7.72 (s, 2H), 7.65 (d, J = 8.4 Hz, 4H), 7.13 (d, J = 9.2 Hz, 8H), 7.03 (d, J = 8.4 Hz, 4H), 6.84 (d, J = 9.0 Hz, 8H), 3.94 (t, J = 1.2 Hz, 8H), 2.96 (t, J = 1.2 Hz, 4H), 1.74–1.90 (m, 14H), 1.51–1.43 (m, 10H), 1.37–1.33 (m, 21H), 0.95–0.89 (m, 14H), 0.88–0.82 (m, 7H) ppm. ^{13}C-NMR (100 MHz, $CDCl_3$): δ = 155.4, 154.7, 147.9, 140.8, 138.7, 138.0, 131.4, 130.6, 128.1, 126.7, 119.6, 115.2, 68.2, 34.7, 31.8, 31.6, 29.3, 29.2, 27.3, 25.8, 22.6, 14.1, 14.0 ppm. HRMS: *m*/*z* calculated for $C_{80}H_{105}O_4N_4$: 1184.8058. Found: 1184.8042 $[M + H]^+$.

3. Results and Discussions

3.1 Synthesis of chromophores DQ1–5

Compounds **DQ1–5** were rationally designed to modulate their relevant electronic and physico-chemical properties. By inserting different electron-donating groups at the 5,8 positions of the quinoxaline core, the HOMO–LUMO energy difference could be tuned, thus effectively modulating their absorption spectra.[38] In addition, the nature of the substituents at the 2,3 positions can affect the electron-accepting capacity of the quinoxaline unit, stabilizing the LUMO orbital.[21] Finally, the presence of alkyl chains on the acceptor and donor groups, other than modifying the electronic and optical properties, can also alter the dispersibility of the fluorophores in the polymer matrix, controlling the potential formation of non-emissive aggregates. Compounds **DQ1–5** (Fig. 1) were synthesized by means of an easy and flexible three-step route, making use of well-known Suzuki–Miyaura cross-coupling reactions as key steps. The two acceptor cores were prepared following a common strategy, shown in Scheme 1. Diamine **2** was synthesized in good yield by the reduction of commercially available 4,7-dibromo-2,1,3-benzothiadiazole (**1**) using a large excess of $NaBH_4$ in EtOH.[17] Compound **2** was used immediately, without purification, for the subsequent step involving a cyclization reaction using diketones **3** or **4**, under slightly different conditions, to obtain quinoxalines **5** and **6**, respectively. The latter were employed in the Suzuki–Miyaura cross-coupling reactions, whose conditions were individually optimized to enhance the yield of each product (Scheme 2).

In particular, compounds **DQ2–4** were synthesized by reacting quinoxalines **5** or **6** with the corresponding boronic acid/ester (**7–9**) in the presence of $Pd(dppf)Cl_2$ as the catalyst and KF as the base under microwave (MW) heating. Compared to conventional heating, MW irradiation allowed shortening the reaction time (approx. 35 minutes at 70 °C) and reducing the number of side-products. A mixture of toluene and MeOH (6/1) was identified as the best medium to absorb microwaves efficiently. However, the MW irradiation conditions were surprisingly ineffective in the synthesis of **DQ1** and **DQ5**. So, **DQ1** was obtained under similar conditions to **DQ2–4** (Scheme 2), but applying conventional heating for 18 h, while **DQ5** was prepared using a synthetic method reported by Kang *et al.* for a different compound.[20] This last reaction was run using $Pd(PPh_3)_4$ and Cs_2CO_3 as the catalyst and base, respectively, at a temperature of 100 °C for 4 hours.

3.2 Spectroscopic characterization in solution

Steady-state UV-vis absorption and fluorescence emission studies. The optical properties of compounds **DQ1–5** were studied in solution by UV-vis absorption and fluorescence emission spectroscopies. The solvent used was toluene because it effectively dissolved all compounds and its refractive index (1.496) is similar to that of PMMA (1.491). Relevant data are presented in Table 1 and Fig. 2. All compounds showed

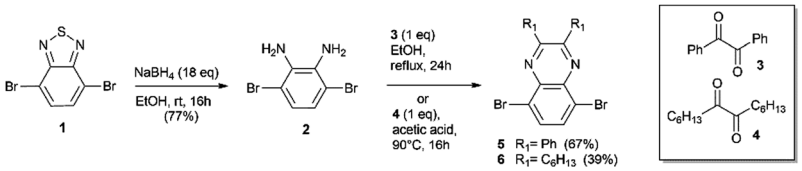

Scheme 1 Synthesis of the quinoxaline cores.

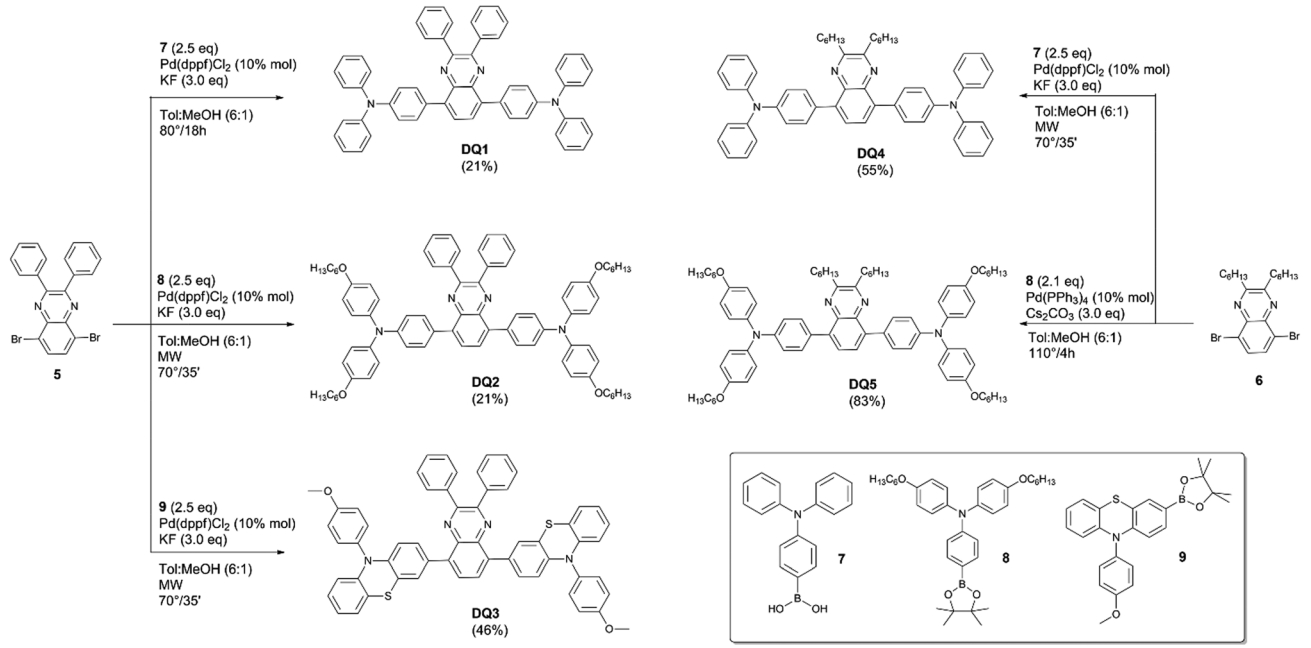

Scheme 2 Synthetic procedures for the preparation of **DQ** fluorophores.

Table 1 Spectroscopic properties of compounds **DQ1–5** in toluene solution

Compound	λ_{abs} (nm)	$\varepsilon \times 10^4$ (M^{-1} cm^{-1})	λ_{emi} (nm)	SS (nm [eV])	$\Phi_f{}^a$ (%)
DQ1	433	3.1	538	105 [0.56]	74
DQ2	457	3.3	567	110 [0.53]	66
DQ3	452	1.2	601	149 [0.68]	46
DQ4	398	1.2	512	117 [0.71]	44
DQ5	416	2.0	529	112 [0.62]	67

[a] Absolute quantum yield of solutions.

maximum absorption wavelengths between 400 nm and 460 nm (Fig. 2, solid lines). Fluorophores **DQ1–3**, having a 2,3-diphenylquinoxaline acceptor core, showed a red-shifted absorption in comparison with the 2,3-dihexylquinoxalines **DQ4–5**. This is consistent with the more extended conjugation provided by the phenyl rings.[21] The maximum absorption wavelength increased from **DQ1** (433 nm) to **DQ3** (452 nm) and then **DQ2** (457 nm), in agreement with the increasing electron-donating characteristics of the lateral groups.[39] The same effect was also found for **DQ4** and **DQ5**.

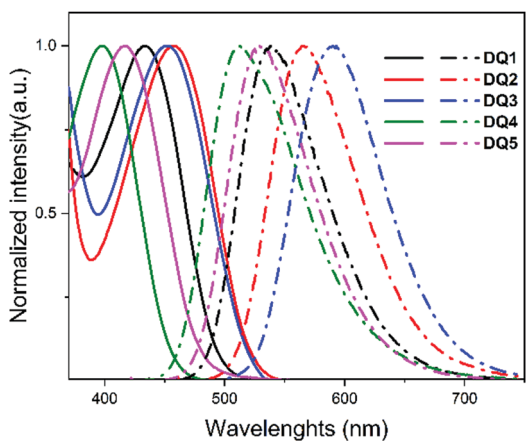

Fig. 2 Normalized absorption spectra (solid lines) and normalized fluorescence emission spectra (dash dot lines) of **DQ1–5** in toluene (0.01 mM) with λ_{exc} at 433, 457, 452, 398 and 416 nm, respectively.

In addition, all the absorption spectra featured broad peaks, maintaining a constant shape at different concentrations (see Fig. S2–S6, ESI†).

The ground-state frontier molecular orbitals of the **DQ** series were calculated using Gaussian 16,[40] Revision C.01 suite of programs, at the B3LYP[41,42]/6-31G* level of theory in toluene.

Solvent effects were included using the polarizable continuum model (PCM).[43] The inspection of the frontier molecular orbitals (see Fig. S1, ESI†) suggests that in all cases, the light absorption in the visible region could involve an internal charge-transfer (ICT) mechanism, as already observed in **DQ1** and similar molecules.[21,44] This is in agreement with the spectroscopic results.

The fluorescence spectra showed an intense emission band between 512 and 600 nm (Fig. 2, dash dot lines), relatively well-matched with the external quantum efficiency of a Si-based PV module. No vibronic structure was observed, and the constant shape of the emission band at different concentrations proved the absence of dye aggregation in toluene for all **DQs** in the explored concentration range (Fig. S2–S6, ESI†). Furthermore, in all cases, large Stokes shifts (0.53–0.71 eV, corresponding to >100 nm) with limited overlap between the absorption and emission spectra were observed, leading to minimal re-absorption phenomena (Table 1).

Transient absorption spectroscopy (TAS) studies. To further characterize the excited states of **DQ1–5** chromophores and

investigate the dynamics of their relaxation after light absorption in toluene solution, femtosecond transient absorption spectroscopy experiments were also carried out. The samples were excited at 400 nm, at the blue edge of absorption of the quinoxaline core, and their transient spectra were recorded in the 0.1 ps–1.5 ns time interval. The results were analysed by simultaneously fitting all the kinetic traces with a combination of exponential functions (global analysis), and using a kinetic scheme based on a sequential decay. Besides kinetic constants, global analysis also retrieves the corresponding spectral components, indicated as evolution associated difference spectra (EADS). The transient absorption spectra of **DQ1–5** recorded in toluene are reported in Fig. 3 and 4, respectively, with the correspondent EADS obtained from global analysis in the bottom panels.

2,3-Diphenyl-substituted compounds **DQ1–3** showed a broad positive excited state absorption (ESA) band, covering almost all the probed spectral interval (Fig. 3a–c). **DQ1** and **DQ2** showed very similar spectra, indicating a minor influence of the alkyl chains on the excited state dynamics, with a small negative band centred at about 440 nm, corresponding to the ground-state bleaching, and a more intense broad positive one, featuring a double-peaked structure because of an evident overlap with the negative stimulated emission (SE) band. In the corresponding EADS panels (Fig. 3d and e), the first component (black line) of both samples presents a broad positive band peaked at 600 nm, living about 2 ps in case of **DQ1** and 700 fs for **DQ2**.

In the following evolution (red lines in Fig. 3d and e), the ESA assumes a double-peaked shape, because of the increase in the positive signal in the 450–500 nm region and the superposition between the broad positive absorption band and the stimulated emission band (peaked at about 530 nm for **DQ1** and 550 nm for **DQ2**). This spectral evolution can be assigned to a fast electronic relaxation of the molecule, as evidenced by a large red-shift of the stimulated emission signal.

According to the theoretical analysis (see Fig. S1, ESI†), the lowest excited state has a charge-transfer character. The positive band above 700 nm noticed in the second EADS could be interpreted in terms of the simultaneous localization of the negative charge on the quinoxaline unit and the positive charge on the triphenylamine donor, as evidenced in previous studies.[45,46] After 14.4 ps for **DQ1** (7.3 ps for **DQ2**), the red component evolves towards the blue EADS.

Although the spectral shape of the third EADS remains mostly unaffected, the stimulated emission signal partially recovers and red-shifts at about 30 nm reflecting a dynamic Stokes-shift due to solvent-induced excited state relaxation. On the same timescale, the band peaked at 600 nm narrows and slightly blue-shifts, as the effect of vibrational cooling occurring in the excited state. The narrowing at 600 nm is particularly evident for **DQ2**. Finally, the signal intensity slightly decreases on the following 448 ps timescale for **DQ1** (540 ps for **DQ2**). For both samples, the final spectral component (green EADS) lives beyond the time interval of the measurement (1.5 ns).

The transient spectrum of **DQ3** appears slightly different as compared to the previously described samples, reflecting the presence of the phenothiazine donor group (Fig. 3c and f), but the excited evolution can be interpreted in a similar way. Also in this case, after a fast electronic relaxation occurring in about 500 fs, a positive band peaked at about 500 nm is observed to increase, together with a broad absorption extending between 600 and >750 nm, and presenting a minimum at about 570 nm, due to the superposition with the stimulated emission band. The band peaked at 500 nm may reflect the localization of positive charge on the phenothiazine ring, while the signal in the red part of the spectrum (>600 nm) can be assigned to the

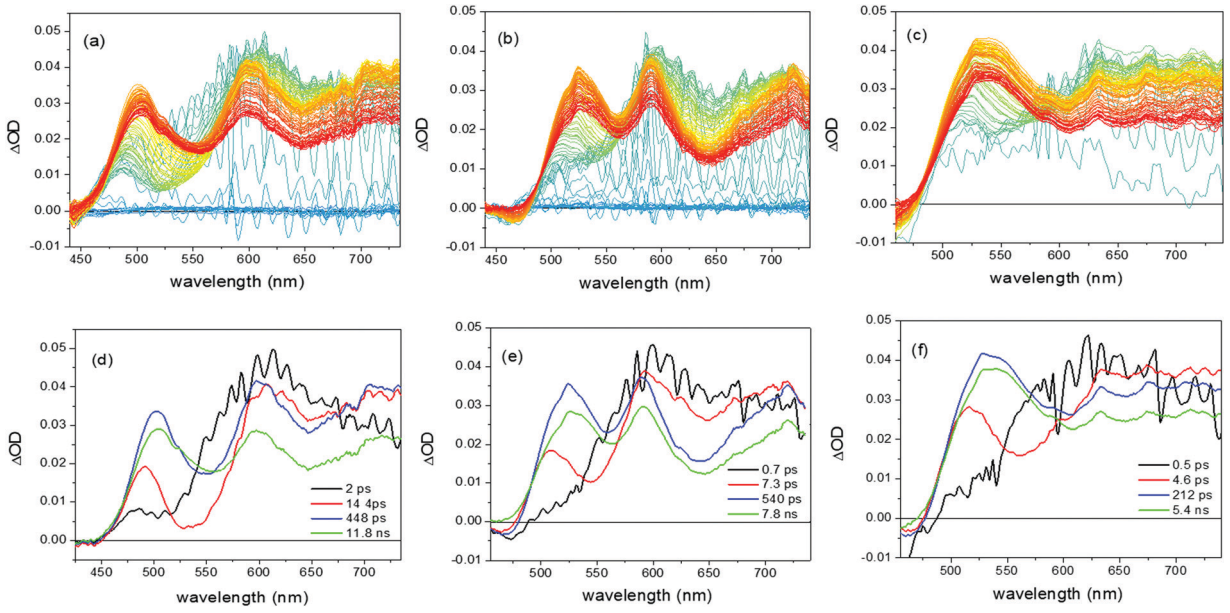

Fig. 3 Transient absorption spectra (a–c) and evolution associated difference spectra (EADS) (d–f) of **DQ1–3** (from left to right) in toluene solutions.

localization of the negative charge on the quinoxaline core, thus confirming the formation of a charge-transfer state also in this case. The spectral dynamics observed on the 5 ps timescale reflects a dynamic Stokes shift of the emission band. The intensity of the overall transient spectrum slightly decreases on the following 212 ps timescale and the final spectral component (green line, Fig. 3f) once again lives longer than the investigated timescale.

The transient absorption spectra and EADS of 2,3-di-*n*-hexylquinoxalines **DQ4** and **DQ5** are reported in Fig. 4. For both samples, a negative band, peaked at about 500 nm, is assigned as the SE signal, and a broad positive ESA band is noticed in the spectra. Opposite to the previous series of compounds, here the spectral evolution observed within the investigated timescale is quite limited. Inspection of the EADS shows a progressive red-shift of the SE band, ascribed to a solvent-induced excited state relaxation, occurring within 10 ps for both samples (evolution from the black to the red component and from the red to the blue one, Fig. 4c and d). The intensity of the ESA band partially decreases in about 325 ps for **DQ4** (about 430 ps for **DQ5**). Already in the second spectral component, a positive band at about 600 nm can be recognized, possibly related to the partial localization of the positive charge on the triphenylamine groups and therefore signalling the emergence of a charge-transfer state upon photoexcitation. Also for these samples, the final spectral component lives longer than the investigated timescale. Overall, the transient absorption spectroscopy measurements of all the investigated compounds confirm the charge-transfer characteristic of the lowest energy excited state, furthermore indicating that no intermediate dark states are involved in its decay, suggesting that its main relaxation channel is of radiative nature, a very beneficial feature for compounds to be employed as LSC emitters.

3.3 Spectroscopic characterization in polymer matrices

DQ luminophores were characterized in polymer matrices by dispersing them in transparent and totally amorphous PMMA and PCMA, obtaining films with a 25 μm ± 5 μm thickness, at different concentrations (0.2–2.2 wt%). All molecules visually showed good dispersion in the polymer matrices, which appeared homogenous and with negligible macroscopic phase separation at the film surface even at the highest fluorophore content (Fig. 5).

Steady-state absorption and emission studies in PMMA. In PMMA films, all **DQs** exhibited broad absorption bands in the 370–550 nm interval (Fig. 6, solid lines and Table 2), with intensity regularly increasing with concentration and without evident differences in the spectral shape (Fig. S7–S11, ESI†). Moreover, no clear absorption bands attributed to the aggregates in polymer films were observed. Fluorescence bands encompassed the 500–700 nm spectral range (Fig. 6 dash dot lines), without evident vibronic contributions even at high doping (Fig. S7–S11, ESI†). The shape of the emission band remained unaltered at different fluorophore concentrations but showed a

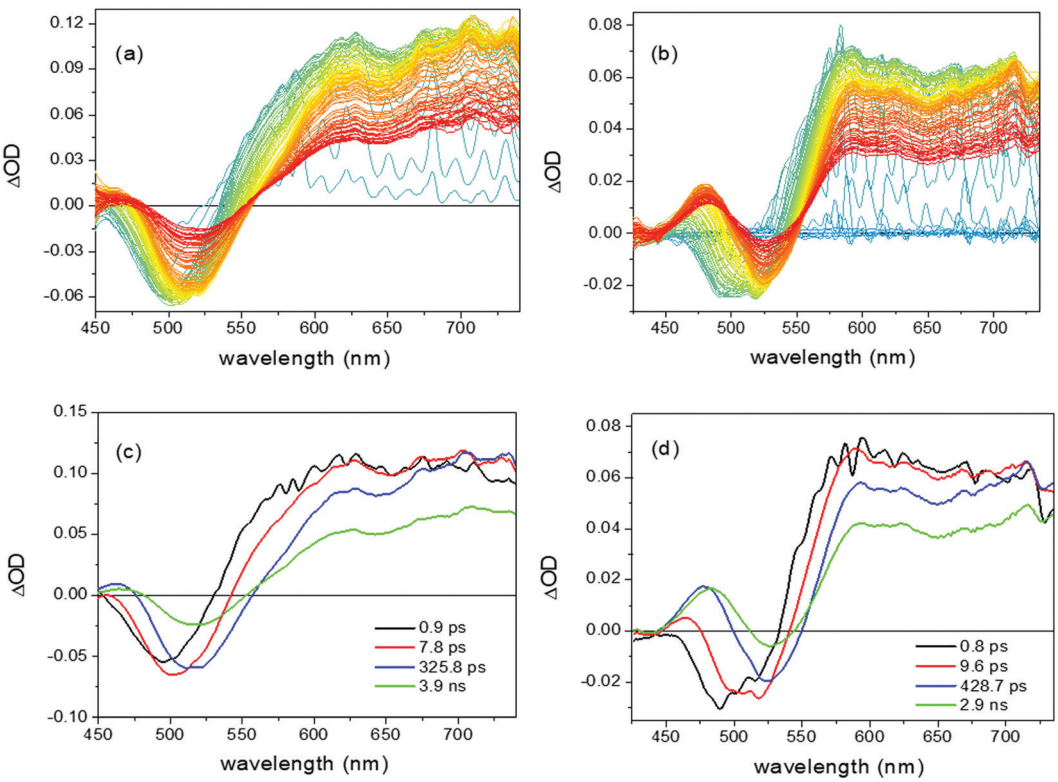

Fig. 4 Transient absorption spectra (a and b) and evolution associated difference spectra (EADS) (c and d) of **DQ4-5** (from left to right) in toluene solutions.

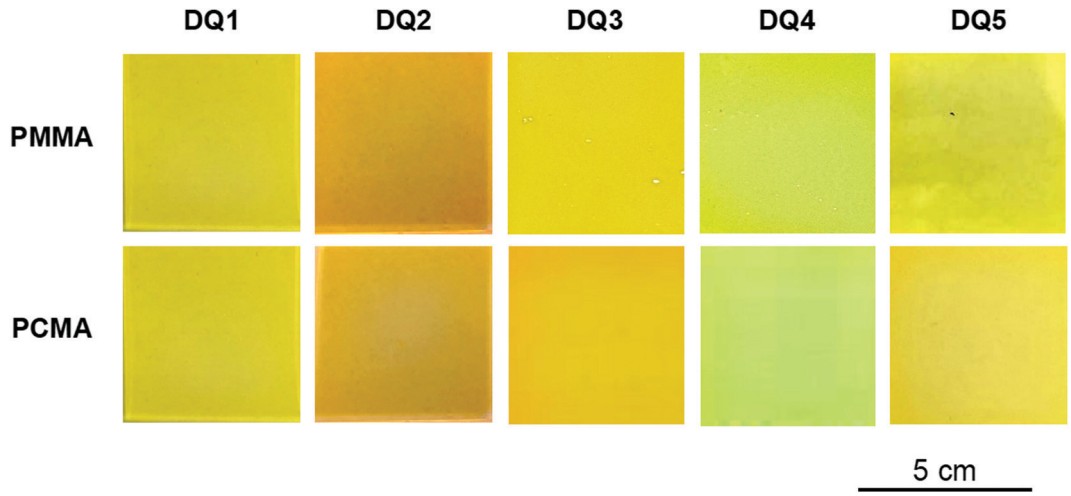

Fig. 5 PMMA and PCMA films doped with **DQ1–5** at 1.4 wt% concentration under visible light illumination.

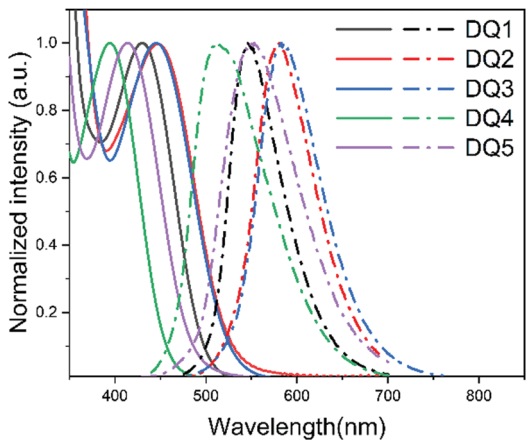

Fig. 6 Normalized absorption spectra (solid lines) and normalized fluorescence emission spectra (dash dot lines) of **DQ1–5** in PMMA (1.0 wt%) with λ_{exc} at 430, 454, 456, 400 and 415 nm, respectively. UV-vis absorption and emission spectra as a function of fluorophore concentration are reported in the ESI† (Fig. S7–S11).

progressive red-shift, possibly caused by moderate auto-absorption phenomena (*i.e.*, inner filter effects).[24,47] Notably, SS of more than 100 nm were observed for all **DQs**/PMMA films. It is worth noting that **DQ1** showed an outstanding fluorescence quantum yield in PMMA (90–97% as compared to 74% in toluene) (Fig. S7, ESI†), seemingly due to the beneficial effect provided by the glassy polymer matrix. This is a typical trend, since entrapment of the fluorophore within the polymer chains can cause a decrease in its conformational freedom, resulting in an increased dissipation of the excited state energy through radiative channels.[48–51] Moreover, no quenching effects were observed up to a concentration of 1.8 wt%, thus suggesting also an excellent compatibility of the fluorophore with the polymer matrix.

This is confirmed by the inspection of epifluorescence microscopy images, revealing the presence of only a few micro-sized fluorophore aggregates with an average size of about 15 μm (Fig. 7), characterized by brilliant emission. Such behaviour appears very promising in obtaining solar collectors with improved optical performances.

Conversely, **DQ2**/PMMA films showed Φ_f values of 30–40% within the entire range of concentrations (Fig. S8, ESI†), lower than those recorded in solutions. No beneficial effect was exerted by the polymer matrix in this case, which can be attributed to the emersion of a large fraction of phase-separated microscopic fluorophore aggregates (Fig. 7). We can hypothesize that, in the initial toluene solution used for film preparation, **DQ2** molecules were well-dispersed. Upon the evaporation of the solvent, their local concentration increased, and thanks to the interaction of their long alkyl chains, they started to form small aggregates, which became progressively entrapped in the polymer matrix. This caused the size of the aggregates to increase, leading to the observed microscopic phase separation (Fig. 7).

The phase dispersion in PMMA also influenced the quantum efficiency of **DQ3**/PMMA and **DQ4**/PMMA films, since the values of 56% and 80% measured at the lowest fluorophore content (0.2 wt%) gradually collapsed with the increasing content to 33% and 58%, respectively (Fig. S9 and S10, ESI†). In these cases, the lower fluorophore compatibility with the PMMA matrix progressively gave rise to the emersion of micro-scale aggregates that, in turn, triggered the activation of the typical ACQ effect (Fig. 7).[52,53]

Table 2 Spectroscopic properties of compounds **DQ1–5** in PMMA and PCMA (1.0 wt%)

	PMMA			PCMA		
Compound	λ_{abs} (nm)	λ_{emi} (nm)	SS (nm [eV])	λ_{abs} (nm)	λ_{emi} (nm)	SS (nm [eV])
DQ1	430	546	116 [0.61]	432	538	106 [0.56]
DQ2	447	580	133 [0.64]	459	569	110 [0.52]
DQ3	446	583	137 [0.65]	449	566	117 [0.57]
DQ4	406	513	107 [0.64]	404	493	89 [0.55]
DQ5	414	553	139 [0.75]	419	519	100 [0.57]

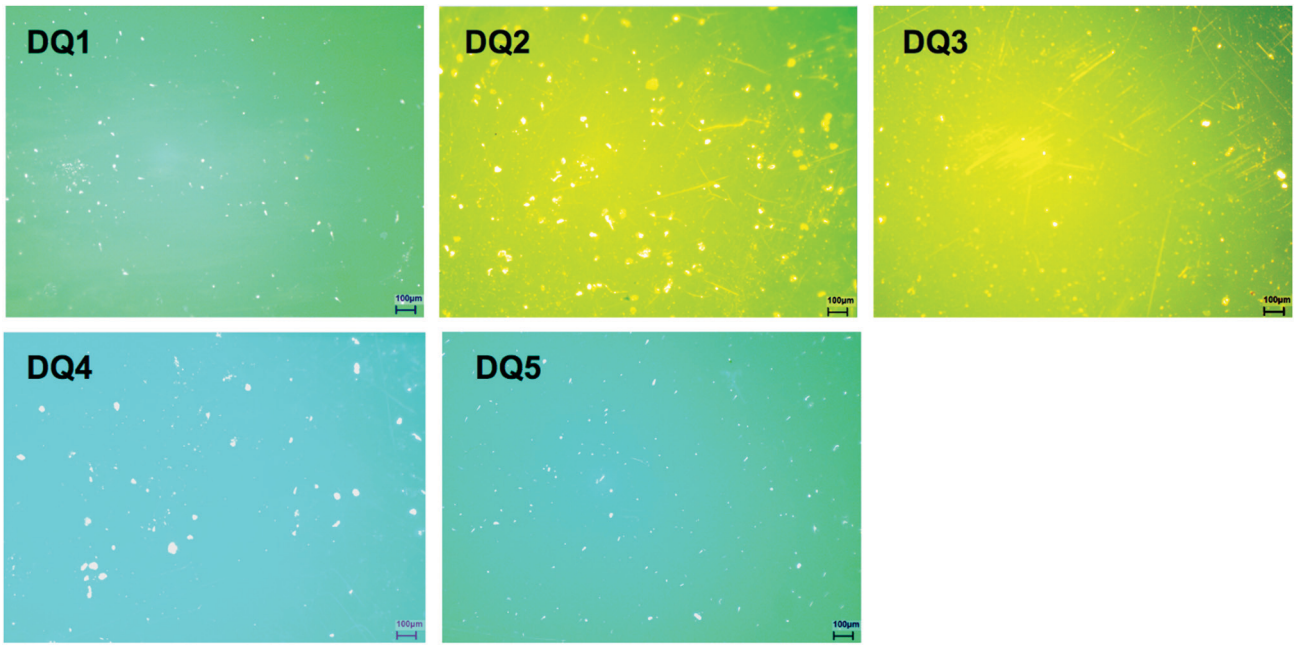

Fig. 7 Fluorescent microscopy images of 1.4 wt% **DQ1–5**/PMMA films. Scale bar = 100 μm.

This phenomenon appeared much less severe in the case of **DQ5**/PMMA films, whose fluorescence quantum yield remained constant at 50–60% in the entire range of investigated concentrations (Fig. S11, ESI†).

Steady-state absorption and emission studies in PCMA. All **DQ** fluorophores were also dispersed in PCMA, which is considered less polar than PMMA due to the stronger aliphatic contribution of the side-chain (Fig. 1).[10] In general, the spectra recorded in PCMA were comparable with those recorded in PMMA, with negligible differences between the peak maxima positions (Fig. 8 and Table 2). In particular, **DQ1–3** films showed absorption maxima increasing with concentration and all the emission bands were affected by red-shifts at high fluorophore concentrations (Fig. S12–S14, ESI†). Significant SS at about 90–120 nm were observed for all molecules, similar to what found in PMMA.

The quantum yields of **DQ1–3** fluorophores appeared generally maintained or increased in the PCMA matrix compared to PMMA. Accordingly, **DQ1**/PCMA films confirmed high values of Φ_f of around 96–98% (Fig. S12, ESI†), whereas a striking increase from 40% to 71% and from 33% to 53% was recorded moving from PMMA to PCMA for **DQ2** (Fig. S13, ESI†) and **DQ3** (Fig. S14, ESI†), respectively, at the highest fluorophore content. This behaviour suggests that a less polar environment increases the phase compatibility between the fluorophores and the polymer matrix, as indicated by the images obtained by fluorescence microscopy of compound **DQ2** in PCMA films (Fig. 9, left). Clearly, a reduced number of smaller **DQ2** aggregates were present in PCMA with respect to the more phase-separated **DQ2**/PMMA system (Fig. 7).

Moving to **DQ4** and **DQ5** (Fig. S15 and S16, ESI†), the introduction of hexyl chains into their acceptor core resulted in a less evident quenching of fluorescence for concentrations higher than 1.4 wt% and in a less pronounced bathochromic shift of the emission maximum. Nevertheless, the alkyl

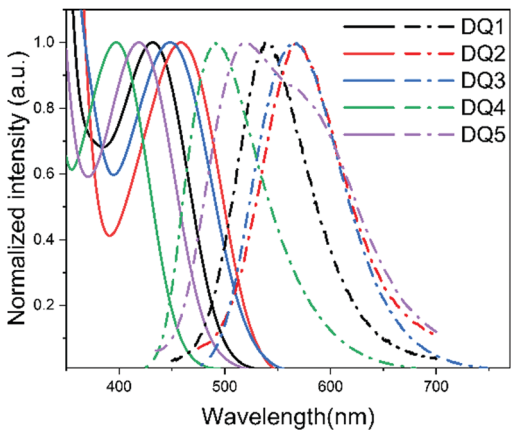

Fig. 8 Normalized absorption spectra (solid lines) and normalized emission spectra (dash dot lines) of **DQ1–5** in PCMA (1.0 wt%) with λ_{exc} at 430, 459, 447, 400, and 419 nm, respectively. UV-vis absorption and emission spectra as a function of fluorophore concentration are reported in the ESI† (Fig. S12–S16).

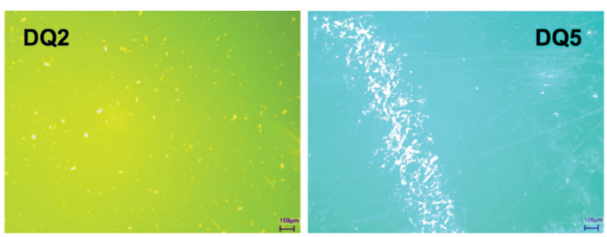

Fig. 9 Fluorescent microscopy images of a 1.4 wt% **DQ2,5**/PCMA film. Scale bar = 100 μm.

characteristic of **DQ4** and **DQ5** affected divergently the Φ_f variations with the fluorophore content. While **DQ4** showed a considerable increase of Φ_f with concentrations (*i.e.*, from 65% at 1.0 wt% to 90% at 1.8 wt%), the quantum yield of **DQ5** declined drastically from 80% at 0.2 wt% to around 53% at 1.8 wt%, *i.e.*, comparable to data gathered from PMMA films at the same content. Φ_f declining in **DQ5**/PCMA films was attributed to the formation of phase-separated aggregates triggering the formation of micro-cracks over the surface of the PCMA film as revealed by fluorescence microscopy (Fig. 9, right). Such hypothesis seems to be confirmed by the emission spectra of **DQ5**/PCMA (Fig. S16, ESI†), where a second emission at a longer wavelength appeared for high concentrations in agreement with the formation of emissive aggregates. Overall, the introduction of alkyl chains into the backbone of the fluorophores seems to promote better dispersion and compatibility with the less polar PCMA matrix, as especially evident in the case of compounds **DQ2** and **DQ4**. Notwithstanding this general observation, **DQ5**, featuring the highest number of alkyl chains of the series, diverges from such behaviour, requiring a more refined explanation.[54,55] Indeed, it must be considered that **DQ5**, despite the flexibility of the *n*-hexyloxy substituents, is the largest molecule among those examined, clearly larger than **DQ1**, but also than **DQ4**. Since the relative motions of the polymer film constituents are restricted, unlike what happens in solutions, it is possible that increasing the concentration of **DQ5** above a certain limit prevented the polymer chains to come sufficiently close due to steric reasons, decreasing the mechanical strength of the films. This caused the appearance of the observed micro-cracks, accompanied by a progressive phase-segregation of the emitter molecules, which was supported by the above-mentioned change in shape of the emission spectra (Fig. S16, ESI†).

Overall, **DQ1** displayed the highest quantum yields in both polymer matrices. Notably, compared to the other compounds studied in this work, **DQ1** does not present either any flexible alkyl substituent on its backbone or phenothiazine substituents, which can assume different conformations due to the bending of the tricyclic system. Therefore, compared to the other compounds, it should be less prone to the non-radiative energy losses resulting from vibrational relaxation of the excited state. This is supported by its relatively low SS value, as can be seen in Table 1, indicative of a lower degree of structural reorganization in the excited state. Finally, from the TAS studies reported in Fig. 3 and 4, it can also be seen that the initial spectral evolution for **DQ1**, assigned to a fast electronic relaxation of the molecule, appears slower than that of the other emitters seem to indicate similar rate constants for all compounds. The variation of Φ_f values with concentrations for all compounds both in the PMMA and PCMA matrices is reported in Fig. 10. All the collected results possibly suggest that even PCMA could experience compatibility issues at the highest fluorophore content of 1.8–2 wt%, which often requires maximizing the solar harvesting features of the LSC collectors. An accessible solution to overcome such an issue would be using copolymers made from methyl methacrylate and cyclohexyl methacrylate to take advantage of both the film stability induced by the former and the effective fluorophore dispersion allowed by the latter. Research efforts aimed at developing these new aspects are currently being pursued in our labs.

Transient absorption spectroscopy studies in polymer matrices. All the transient absorption spectra of the samples dispersed in the polymer appeared very similar (Fig. S17 and S18, ESI†): an intense and broad positive excited state absorption band was observed soon after excitation, covering the most of the spectrum. The intensity of the signal gradually decreases in time, without significant spectral evolution.

The dynamic Stokes shift observed in solution is barely observed in the matrix, because of the lower vibrational freedom and more constrained geometry experienced by the molecules in such an environment. The intensity of the absorption signal decayed bi-exponentially in all **DQ** samples, with the excited state showing a relatively long lifetime of >1.5 ns. Overall, these measurements show that the excited state relaxation is dominated by the radiative channel also in the polymer, and that

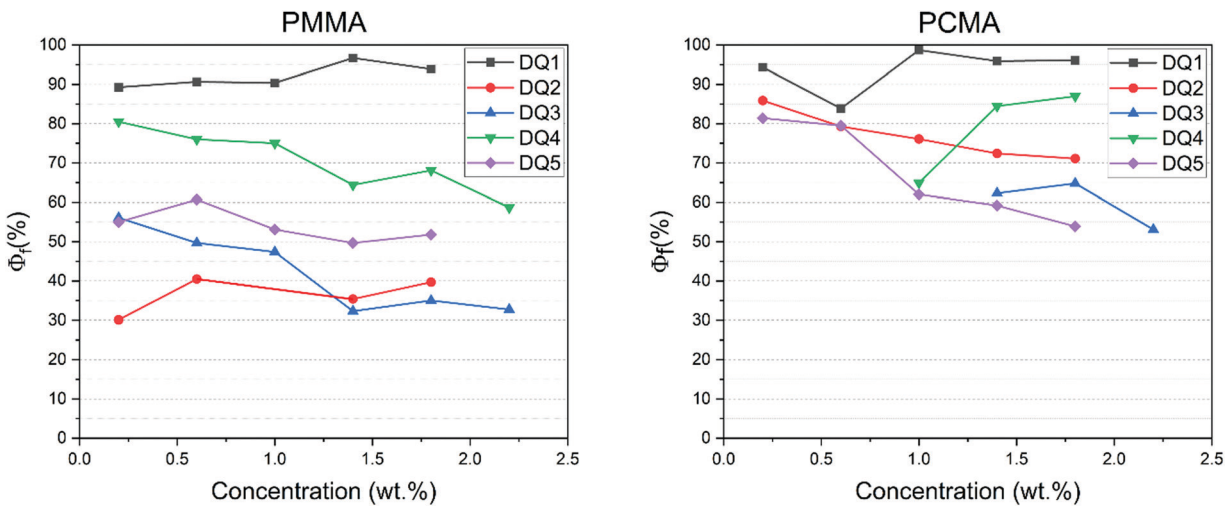

Fig. 10 Φ_f values (%) of the PMMA (left) and PCMA (right) films tested at different fluorophore concentrations.

the variation in Φ_f observed when moving from the solution to the solid phase can mainly be associated with both the more restricted conformation adopted by the different molecules in the polymer and the degree of dispersibility of the various compounds in the matrix. To demonstrate the effect of the matrix, which can also induce a decreased emission efficiency in the case of suboptimal compatibility, Fig. 11 reports the comparison of the kinetic traces measured at the maximum of the excited state absorption band (640 nm) for **DQ5** in toluene and in the two polymer matrices, PMMA and PCMA (1.0 wt%). It is evident that the fast decay component has a higher weight in the polymers compared to the solution, which affects the overall Φ_f observed in the different environments. This is most probably due to the lower conformational freedom experienced by the molecules in the polymer matrix, which reduces the degrees of structural rearrangement in the excited state, as also evidenced by the reduced dynamic Stokes shift of the stimulated emission band (see Fig. S17 and S18, ESI†). To complete the characterization of the films, fluorescence lifetime measurements have also been performed for all compounds dispersed in PMMA at 1.0 wt% concentration. The fluorescence decay rates are similar for all compounds, with lifetimes in the 4–8 ns time range, quite typical of organic fluorophores. Fluorescence lifetimes are slightly shorter for **DQ4** and **DQ5** if compared to the other molecules. We found that the best fitting results (with a χ^2 value of about 1) were obtained for a bi-exponential decay: this could reflect either the presence of small inhomogeneities in the chemical environment surrounding the fluorophore molecules or the formation of oligomers with slightly different decay rates. The fluorescence decay curves and lifetimes are reported in the ESI† (Fig. S19 and Table S1).

3.4 LSC performances

Before determining the photon efficiencies of the prepared thin-film LSCs, auto-absorption in the active film was analysed. The measurements were performed by irradiating the surface of the selected devices with a laser (λ_{exc} = 405 nm, 1 mW cm^{-2})

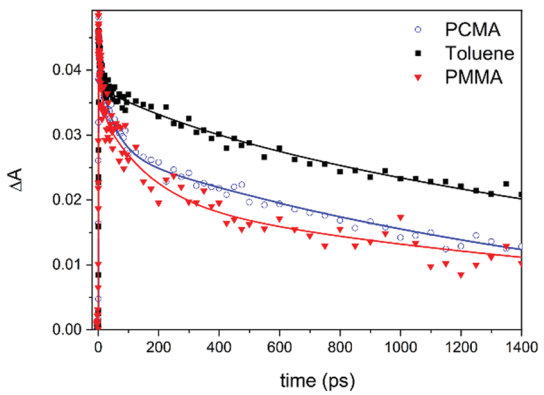

Fig. 11 Comparison of the kinetic trace at 640 nm measured for **DQ5** in toluene (black squares); PCMA (blue open circles); PMMA (red filled triangles). Continuous lines represent fit from global analysis. The associated time constants are reported in Fig. 4(d), Fig. S18.1(d) and S182(b) (ESI†).

and the edge-emitted power was recorded as a function of the optical pathlength distance between the excitation spot and the collecting edge (Fig. S21, ESI†). LSCs based on **LR305**, **DQ1** and **DQ4** were evaluated. **LR305** was selected to be as the state-of-the-art fluorophore in LSC, while **DQ1** and **DQ4** as fluorophores with top and intermediate fluorescence quantum efficiencies, as reported in Figure 10. Fluorophore content was selected in terms of the maximum absolute Φ_f, *i.e.*, 1.4 wt% for **DQ1** and **DQ4**. As far as **LR305** is concerned, the concentration of 1.0 wt% was selected in terms of the maximum LSC performance as determined in a previous study.[8]

Notably, as the optical pathlength distance increased, the edge-emitted power was found to progressively decrease in all cases (Fig. S21a, ESI†). This phenomenon appeared more evident for the LSC based on **LR305**, possibly due to the lowest SS of 36 nm[27] compared to 106 nm for **DQ1** and 89 nm for **DQ4**. Moreover, by comparing the collected emission spectra, an evident red-shift of about 20 nm in the emission maximum was observed in the case of **LR305**, thus supporting emission losses by the occurrence of reabsorption phenomena (Fig. S21b, ESI†).

The optical performances of LSC based on **LR305**, **DQ1** and **DQ4** were then evaluated in terms of the internal and external photon efficiency (η_{int} and η_{ext}, respectively) (Table 3). η_{int} and η_{ext} were obtained according to the recently published protocols[35] and calculated from eqn (S1) and (S2) (ESI†). In detail, η_{int} represents the ratio of photons collected at the LSC edges to the number of absorbed photons by the embedded fluorophores, and it is a key parameter to determine all lightguide losses. η_{ext} is the ratio of photons collected at the LSC edges to the number of total incident photons, and it also provides information about the solar harvesting features of the device.

It is worth noting that for both the η_{int} and η_{ext} parameters, **DQ1** was the best fluorophore in providing the highest LSC efficiencies with values of 42.9% and 6.2%, respectively. Surprisingly, the η_{int} of the LSC based on **LR305** resulted the lowest (16.6%). According to the η_{int} determination, the broadest absorption band of **LR305** adversely affects this parameter in largest extent.

Conversely, η_{ext} shows a different trend of performances, *i.e.*, with **DQ1** as the best fluorophore followed by the state-of-the-art **LR305**. **DQ4**, notwithstanding the higher but similar Φ_f values (64.4 against 59.3%), possibly suffers from inferior solar harvesting characteristics with respect to the perylene bisimide chromophore.

Moreover, the photon efficiencies obtained here appear to be higher than those reported in a recent study.[56] Overall, **DQ1** turns out to be a very promising fluorophore for employment in LSCs.

However, for LSC practical applications, **DQ1**/PMMA stability must be assessed through performance measurements over time.

Table 3 Best Φ_f (%) and optical performances obtained for fluorophores **DQ1** and **DQ4** dispersed in PMMA in comparison with **LR305**

Chromophore	Matrix	Concentration (wt%)	Φ_f (%)	η_{int} (%)	η_{ext} (%)
LR305	PMMA	1.0	59.3	16.6	4.7
DQ1	PMMA	1.4	96.7	42.9	6.2
DQ4	PMMA	1.4	64.4	27.9	3.6

Notably, **DQ1**/PMMA films did not show any noticeable variation in their visible appearance following their preparation, and with optical performances maintained over months. Also, the thermal stability of the fluorophore was evaluated through thermogravimetric analysis showing that the samples maintained at least 95% of their weight up to 300 °C (Fig. S25, ESI†). The photostability of **DQ1**/PMMA LSCs was then preliminarily investigated by continuously irradiating a 0.25 cm^2 spot of the film at 430 nm with a 450 W Xe arc lamp under aerobic conditions. The film samples were placed in the spectrofluorometer chamber and fixed in the solid-state holder, thus receiving irradiances of about 50 μW cm^{-2}. Notably, **DQ1** retained 97.8% of its emission after two hours of continuous excitation compared to the 98.8% of **LR305** (Fig. S26, ESI†), thus suggesting a potentially sufficient photostability. Further experiments will be carried out in order to definitely assess this behaviour.

4. Conclusions

In conclusion, we have reported the preparation of thin-film LSCs having optical properties superior to those of the state-of-the-art solar collectors. This result was obtained by replacing the reference fluorophore **LR305** in PMMA and PCMA films with a series of new high quantum yield, donor–acceptor–donor (D–A–D) photostable fluorophores (**DQ1–5**) characterized by a central quinoxalinic acceptor core and triarylamines or phenothiazine as donor groups. Thanks to their structures, all fluorophores presented excited states characterized by a high degree of intramolecular charge transfer, which was confirmed by both DFT computational analysis and transient absorption spectroscopy studies. Notably, they displayed intense emissions between 550 and 600 nm with Stokes shifts at about 80–120 nm that helped in minimizing the auto-absorption effects when dispersed in polymers at high content. Furthermore, decoration with long alkyl chains at different parts of the molecular backbone allowed tuning their dispersibility in polymer films. It is worth noting that **DQ1** in PMMA provided outstanding LSC η_{int} and η_{ext} values of 42.9 and 6.2%, respectively. This result was addressed to the effective combination between high phase compatibility and excellent quantum yield, which for **DQ1** reached remarkable values of >95% in both PMMA and PCMA matrices.

In view of these performances, our findings provide new advances for the widespread distribution of the LSC/PV system in the integrated photovoltaics, which is the backbone of the zero-energy building European target.

Conflicts of interest

There are no conflicts to declare.

Acknowledgements

We thank ''Regione Toscana'' (COLOURS project, POR FESR 2014-2020, grant no. 3553.04032020.158000411) and ''Fondazione Cassa di Risparmio di Firenze'' (SUNNYSIDE project, grant no. 2020.1408) for financial support. A. S. and C. C. acknowledge MIUR Grant – Department of Excellence 2018–2022. Computational resources were provided by hpc@dbcf (http://molsys.dbcf.unisi.it/hpc). MDD and MT acknowledge European Union's Horizon 2020 research and innovation program under grant agreement no. 871124 Laserlab-Europe. Dr Giulia Tuci (CNR-ICCOM) and Mr Francesco Ventura are kindly acknowledged for their help in TGA experiments and fluorescence microscopy, respectively. The Mass Spectrometry Center (CISM) of the University of Florence is kindly acknowledged for HRMS analyses.

Notes and references

1 N. Armaroli and V. Balzani, *Chem. – Eur. J.*, 2016, **22**, 32–57.
2 G. M. Wilson, M. Al-Jassim, W. K. Metzger, S. W. Glunz, P. Verlinden, G. Xiong, L. M. Mansfield, B. J. Stanbery, K. Zhu, Y. Yan, J. J. Berry, A. J. Ptak, F. Dimroth, B. M. Kayes, A. C. Tamboli, R. Peibst, K. Catchpole, M. O. Reese, C. S. Klinga, P. Denholm, M. Morjaria, M. G. Deceglie, J. M. Freeman, M. A. Mikofski, D. C. Jordan, G. TamizhMani and D. B. Sulas-Kern, *J. Phys. D: Appl. Phys.*, 2020, **53**, 493001.
3 J. S. Batchelder, A. H. Zewai and T. Cole, *Appl. Opt.*, 1979, **18**, 3090.
4 W. H. Weber and J. Lambe, *Appl. Opt.*, 1976, **15**, 2299.
5 J. Roncali, *Adv. Energy Mater.*, 2020, **10**, 2001907.
6 F. Meinardi, F. Bruni and S. Brovelli, *Nat. Rev. Mater.*, 2017, **2**, 17072.
7 G. Griffini, *Front. Mater.*, 2019, **6**, 29.
8 F. J. Ostos, G. Iasilli, M. Carlotti and A. Pucci, *Polymers*, 2020, **12**, 2898.
9 T. M. Clarke, K. C. Gordon, W. M. Kwok, D. L. Phillips and D. L. Officer, *J. Phys. Chem. A*, 2006, **110**, 7696–7702.
10 C. Papucci, A. Dessì, C. Coppola, A. Sinicropi, G. Santi, M. di Donato, M. Taddei, P. Foggi, L. Zani, G. Reginato, A. Pucci, M. Calamante and A. Mordini, *Dyes Pigm.*, 2021, **188**, 109207.
11 H. J. Song, D. H. Kim, E. J. Lee and D. K. Moon, *J. Mater. Chem. A*, 2013, **1**, 6010–6020.
12 B. Li, M. Zhao and F. Zhang, *ACS Mater. Lett.*, 2020, **2**, 905–917.
13 P. Y. Gu, J. Zhang, G. Long, Z. Wang and Q. Zhang, *J. Mater. Chem. C*, 2016, **4**, 3809–3814.
14 L. Lyu, R. Su, S. Y. Al-Qaradawi, K. A. Al-Saad and A. El-Shafei, *Dyes Pigm.*, 2019, **171**, 107683.
15 W. Liu, Z. Liu, J. Yan, L. Wang, H. Xu, H. Wang and B. Zhao, *Dyes Pigm.*, 2021, **191**, 109305.
16 D. Gedefaw, M. Prosa, M. Bolognesi, M. Seri and M. R. Andersson, *Adv. Energy Mater.*, 2017, **7**, 1700575.
17 M. L. Jiang, J. Wen, Z. Chen, W. Tsai, T. Lin, T. J. Chow and Y. J. Chang, *ChemSusChem*, 2019, **12**, 3654–3665.
18 B. D. Lindner, Y. Zhang, S. Höfle, N. Berger, C. Teusch, M. Jesper, K. I. Hardcastle, X. Qian, U. Lemmer, A. Colsmann, U. H. F. Bunz and M. Hamburger, *J. Mater. Chem. C*, 2013, **1**, 5718–5724.

19 H. Zhang, Y. Wu, W. Zhang, E. Li, C. Shen, H. Jiang, H. Tian and W. H. Zhu, *Chem. Sci.*, 2018, **9**, 5919–5928.
20 H. J. Son, W. S. Han, D. H. Yoo, K. T. Min, S. N. Kwon, J. Ko and S. O. Kang, *J. Org. Chem.*, 2009, **74**, 3175–3178.
21 Y. Chen, Y. Ling, L. Ding, C. Xiang and G. Zhou, *J. Mater. Chem. C*, 2016, **4**, 8496–8505.
22 T. A. Geervliet, I. Gavrila, G. Iasilli, F. Picchioni and A. Pucci, *Chem. – Asian J.*, 2019, **14**, 877–883.
23 R. Mori, G. Iasilli, M. Lessi, A. B. Muñoz-García, M. Pavone, F. Bellina and A. Pucci, *Polym. Chem.*, 2018, **9**, 1168–1177.
24 J. Lucarelli, M. Lessi, C. Manzini, P. Minei, F. Bellina and A. Pucci, *Dyes Pigm.*, 2016, **135**, 154–162.
25 G. Iasilli, R. Francischello, P. Lova, S. Silvano, A. Surace, G. Pesce, M. Alloisio, M. Patrini, M. Shimizu, D. Comoretto and A. Pucci, *Mater. Chem. Front.*, 2019, **3**, 429–436.
26 F. De Nisi, R. Francischello, A. Battisti, A. Panniello, E. Fanizza, M. Striccoli, X. Gu, N. L. C. Leung, B. Z. Tang and A. Pucci, *Mater. Chem. Front.*, 2017, **1**, 1406–1412.
27 M. Carlotti, E. Fanizza, A. Panniello and A. Pucci, *Sol. Energy*, 2015, **119**, 452–460.
28 G. Albano, T. Colli, T. Biver, L. A. Aronica and A. Pucci, *Dyes Pigm.*, 2020, **178**, 108368.
29 G. Albano, T. Colli, L. Nucci, R. Charaf, T. Biver, A. Pucci and L. A. Aronica, *Dyes Pigm.*, 2020, **174**, 108100.
30 P. L. Gentili, M. Mugnai, L. Bussotti, R. Righini, P. Foggi, S. Cicchi, G. Ghini, S. Viviani and A. Brandi, *J. Photochem. Photobiol., A*, 2007, **187**, 209–221.
31 M. Di Donato, A. Iagatti, A. Lapini, P. Foggi, S. Cicchi, L. Lascialfari, S. Fedeli, S. Caprasecca and B. Mennucci, *J. Phys. Chem. C*, 2014, **118**, 23476–23486.
32 E. R. Henry, *Biophys. J.*, 1997, **72**, 652–673.
33 I. H. M. Van Stokkum, D. S. Larsen and R. Van Grondelle, *Biochim. Biophys. Acta, Bioenerg.*, 2004, **1657**, 82–104.
34 J. J. Snellenburg, S. Laptenok, R. Seger, K. M. Mullen and I. H. M. van Stokkum, *J. Stat. Softw.*, 2012, **49**, 1–22.
35 M. G. Debije, R. C. Evans and G. Griffini, *Energy Environ. Sci.*, 2021, **14**, 293–301.
36 C. Yang, D. Liu and R. R. Lunt, *Joule*, 2019, **3**, 2871–2876.
37 B. Mátravölgyi, T. Hergert, A. Thurner, B. Varga, N. Sangiorgi, R. Bendoni, L. Zani, G. Reginato, M. Calamante, A. Sinicropi, A. Sanson, F. Faigl and A. Mordini, *Eur. J. Org. Chem.*, 2017, 1843–1854.
38 G. Qian, B. Dai, M. Luo, D. Yu, J. Zhan, Z. Zhang, M. Dongge and Z. Y. Wang, *Chem. Mater.*, 2008, **20**, 6208–6216.
39 A. Dessì, M. Calamante, A. Mordini, M. Peruzzini, A. Sinicropi, R. Basosi, F. Fabrizi De Biani, M. Taddei, D. Colonna, A. Di Carlo, G. Reginato and L. Zani, *RSC Adv.*, 2015, **5**, 32657–32668.
40 M. J. Frisch, G. W. Trucks, H. B. Schlegel, G. E. Scuseria, M. A. Robb, J. R. Cheeseman, G. Scalmani, V. Barone, G. A. Petersson, H. Nakatsuji, X. Li, M. Caricato, A. V. Marenich, J. Bloino, B. G. Janesko, R. Gomperts, B. Mennucci, H. P. Hratchian, J. V. Ortiz, A. F. Izmaylov, J. L. Sonnenberg, D. Williams-Young, F. Ding, F. Lipparini, F. Egidi, J. Goings, B. Peng, A. Petrone, T. Henderson, D. Ranasinghe, V. G. Zakrzewski, J. Gao, N. Rega, G. Zheng, W. Liang, M. Hada, M. Ehara, K. Toyota, R. Fukuda, J. Hasegawa, M. Ishida, T. Nakajima, Y. Honda, O. Kitao, H. Nakai, T. Vreven, K. Throssell, J. A. Montgomery Jr, J. E. Peralta, F. Ogliaro, M. J. Bearpark, J. J. Heyd, E. N. Brothers, K. N. Kudin, V. N. Staroverov, T. A. Keith, R. Kobayashi, J. Normand, K. Raghavachari, A. P. Rendell, J. C. Burant, S. S. Iyengar, J. Tomasi, M. Cossi, J. M. Millam, M. Klene, C. Adamo, R. Cammi, J. W. Ochterski, R. L. Martin, K. Morokuma, O. Farkas, J. B. Foresman and D. J. Fox, *GAUSSIAN16: Gaussian 16, Revision C.01*, Gaussian, Inc., Wallingford CT, 2016.
41 A. D. Becke, *J. Chem. Phys.*, 1993, **98**, 5648–5652.
42 C. Lee, W. Yang and R. G. Parr, *Phys. Rev. B: Condens. Matter Mater. Phys.*, 1988, **37**, 785–789.
43 J. Tomasi, B. Mennucci and R. Cammi, *Chem. Rev.*, 2005, **105**, 2999–3093.
44 X. Lu, S. Fan, J. Wu, X. Jia, Z.-S. Wang and G. Zhou, *J. Org. Chem.*, 2014, **79**, 6480–6489.
45 K. Lušpai, A. Staško, V. Lukeš, D. Dvoranová, Z. Barbieriková, M. Bella, V. Milata, P. Rapta and V. Brezová, *J. Solid State Electrochem.*, 2015, **19**, 113–122.
46 K. Y. Chiu, T. X. Su, J. H. Li, T. H. Lin, G. S. Liou and S. H. Cheng, *J. Electroanal. Chem.*, 2005, **575**, 95–101.
47 F. Donati, A. Pucci, C. Cappelli, B. Mennucci and G. Ruggeri, *J. Phys. Chem. B*, 2008, **112**, 3668–3679.
48 J. M. Drake, M. L. Lesiecki, J. Sansregret and W. R. L. Thomas, *Appl. Opt.*, 1982, **21**, 2945.
49 M. G. Debije and P. P. C. Verbunt, *Adv. Energy Mater.*, 2012, **2**, 12–35.
50 J. Donovalová, M. Cigáň, H. Stankovičová, J. Gašpar, M. Danko, A. Gáplovský and P. Hrdlovič, *Molecules*, 2012, **17**, 3259–3276.
51 M. Kaholek and P. Hrdlovič, *J. Photochem. Photobiol., A*, 1997, **108**, 283–288.
52 F. Gianfaldoni, F. De Nisi, G. Iasilli, A. Panniello, E. Fanizza, M. Striccoli, D. Ryuse, M. Shimizu, T. Biver and A. Pucci, *RSC Adv.*, 2017, **7**, 37302–37309.
53 C. Papucci, T. A. Geervliet, D. Franchi, O. Bettucci, A. Mordini, G. Reginato, F. Picchioni, A. Pucci, M. Calamante and L. Zani, *Eur. J. Org. Chem.*, 2018, 2657–2666.
54 A. Pucci, N. Tirelli, G. Ruggeri and F. Ciardelli, *Macromol. Chem. Phys.*, 2005, **206**, 102–111.
55 N. Tirelli, S. Amabile, C. Cellai, A. Pucci, L. Regoli, G. Ruggeri and F. Ciardelli, *Macromolecules*, 2001, **34**, 2129–2137.
56 F. Corsini, A. Nitti, E. Tatsi, G. Mattioli, C. Botta, D. Pasini and G. Griffini, *Adv. Opt. Mater.*, 2021, **9**, 2100182.